

Accurate and thermodynamically consistent hydrogen equation of state for planetary modeling with flow matching

Hao Xie,¹ Saburo Howard,¹ and Guglielmo Mazzola¹

¹*Department of Astrophysics, University of Zürich, Winterthurerstrasse 190, 8057 Zürich, Switzerland*

(Dated: January 22, 2025)

Accurate determination of the equation of state of dense hydrogen is essential for understanding gas giants. Currently, there is still no consensus on methods for calculating its entropy, which play a fundamental role and can result in qualitatively different predictions for Jupiter’s interior. Here, we investigate various aspects of entropy calculation for dense hydrogen based on *ab initio* molecular dynamics simulations. Specifically, we employ the recently developed flow matching method to validate the accuracy of the traditional thermodynamic integration approach. We then clearly identify pitfalls in previous attempts and propose a reliable framework for constructing the hydrogen equation of state, which is accurate and thermodynamically consistent across a wide range of temperature and pressure conditions. This allows us to conclusively address the long-standing discrepancies in Jupiter’s adiabat among earlier studies, demonstrating the potential of our approach for providing reliable equations of state of diverse materials.

Introduction. The equation of state (EOS) of dense hydrogen (H) is one of the core ingredients to model the internal structure of giant gaseous planets, such as Jupiter and Saturn [1]. With the wealth of data from recent spacecraft missions, Galileo [2] and Juno [3], which measured Jupiter’s atmospheric composition and gravitational field, lack of accurate knowledge of the thermodynamic properties of hydrogen is now considered as one of the major roadblocks in planetary science [4–7]. As parameterized planetary models already require several hypotheses [5, 8–10], an uncontested EOS is needed to advance the field.

Since the high temperature and pressure inside these planets are still largely beyond the reach of current experimental techniques, one usually relies instead on numerical simulations, typically *ab initio* molecular dynamics (MD) based on electron structure methods such as density functional theory (DFT) or quantum Monte Carlo (QMC). Up to now, there have been several widely used *ab initio* EOSs for planetary science applications, including the one by Chabrier, Mazevet and Soubiran (CMS19) [11], by Militzer and Hubbard (MH13) [12], and the Rostock EOS (REOS2 [13], REOS3 [14]) of various versions. All of them are derived from DFT-MD simulations using the exchange-correlation functional of Perdew, Burke and Ernzerhof (PBE) [15]. Despite this common origin, however, they can make significant differences in the resulting Jupiter model, such as the location of adiabat and the predicted size of core mass [4, 7].

The key factor behind these discrepancies of planetary models is the calculation of entropy, which has been recognized and discussed to some extent in several studies [4, 6, 12]. Unlike observables such as energy E and pressure p , the Helmholtz free energy F and entropy $S = (E - F)/T$ are not directly accessible from *ab initio* simulations and often rely on extra procedures called thermodynamic integration (TI). One common implementation of this technique involves interpolating the available data to create a continuous path on the temperature-density phase diagram [4, 13]. From basic

statistical mechanics we have

$$\left(\frac{\partial F}{\partial T}\right)_\rho = -\frac{E}{T^2}, \quad \left(\frac{\partial F}{\partial \rho}\right)_T = \frac{p}{\rho^2 T}. \quad (1)$$

These two equations correspond to integrating the energy (pressure) of the system along isochores (isotherms), respectively. However, this approach has been criticized because, due to limited number of simulation points in practice, the interpolation procedure may introduce uncontrollable systematic errors [12].

An alternative TI scheme is called the coupling constant integration (CCI) [16, 17] or Hamiltonian thermodynamic integration [18]. By connecting the target state to an artificial Hamiltonian with tractable thermodynamic properties, this method further allows for the calculation of *absolute* entropy. However, it is also much more expensive due to the need to perform additional MD simulations, and therefore only suitable for investigating a small region of the phase diagram [12, 19]. Besides, one has to carefully choose relevant parameters in the artificial system and MD simulations to ensure well-converged results [20], and the errors associated with discrete simulation points still remain.

The uncertainties involved in entropy calculation are further exacerbated by the fact that the EOS used for planetary modeling is usually composed of several parts, each based on different theoretical approach and has different phase region of validity. For example, although DFT-MD can provide a good description of electron correlations at intermediate temperatures and densities, especially near pressure-induced dissociation, it will quickly become inefficient at lower densities $\rho \lesssim 0.2\text{g/cm}^3$. For such a region deep within the molecular phase, empirical chemical models such as the well known Saumon–Chabrier–van Horn (SCvH) EOS [21] are generally believed to be accurate and reliable. In practice, the data from these different methods needs to be connected in some way. This, however, could possibly introduce critical errors, as we will demonstrate below.

In this Letter, we focus on the crucial issue of entropy calculation at the DFT-PBE level of theory, aiming to resolve

long-standing disagreements among various Jupiter model predictions, which are highly sensitive to small changes in entropy [4, 6, 12, 22]. We rely solely on *ab initio* theory and well-established experimental data without invoking indirect observations. The purpose of this paper is not to reconcile planetary models with spacecraft measurements [1, 5], but rather to provide a non-parametric hydrogen EOS, ranging from roughly 1 bar to 700GPa, that forms a solid foundation for future model revisions.

We calculate the free energy and entropy of dense hydrogen using a recently developed method called *flow matching* [23–25]. Unlike the demonstrative example shown in Ref. [26], here the calculations are based on DFT-MD simulations and thus have *ab initio* accuracy. Basically, we employ a machine-learned invertible transformation f , which acts on configuration samples $\mathbf{x} \equiv (\mathbf{r}_1, \dots, \mathbf{r}_N)$ of the N proton coordinates, to directly connect two phase points $(T_0, \rho_0), (T_1, \rho_1)$ of interest. Given the transformation can bring the two states close enough to ensure a sufficient overlap, their free energy difference (scaled by temperature) can then be efficiently estimated as follows:

$$\beta_1 F_1 - \beta_0 F_0 = -\ln \mathbb{E}_{\mathbf{x} \sim p_0(\mathbf{x})} \left[e^{-\Phi_{\rightarrow}(\mathbf{x})} \right] = \ln \mathbb{E}_{\mathbf{x} \sim p_1(\mathbf{x})} \left[e^{\Phi_{\leftarrow}(\mathbf{x})} \right], \quad (2)$$

where $p_i(\mathbf{x}) \propto e^{-\beta_i E_i(\mathbf{x})}$ ($i = 0, 1$) are the corresponding Boltzmann distributions, $\beta_i = 1/k_B T_i$, k_B being the Boltzmann constant, and

$$\Phi_{\rightarrow}(\mathbf{x}) = \beta_1 E_1(f(\mathbf{x})) - \beta_0 E_0(\mathbf{x}) - \ln \left| \det \left(\frac{\partial f(\mathbf{x})}{\partial \mathbf{x}} \right) \right|, \quad (3a)$$

$$\Phi_{\leftarrow}(\mathbf{x}) = \beta_1 E_1(\mathbf{x}) - \beta_0 E_0(f^{-1}(\mathbf{x})) + \ln \left| \det \left(\frac{\partial f^{-1}(\mathbf{x})}{\partial \mathbf{x}} \right) \right|, \quad (3b)$$

are known as the *forward* and *reverse* work, respectively [27]. In practice, the two estimators in Eq. (2) provide both upper and lower bound of the free energy difference, which can be pretty tight [27]. In this way, one can accurately estimate the entropy difference based solely on samples and energy functions of the two end states, thus avoid errors arising from any kinds of interpolation between them as done in TI. Moreover, it is also fairly straightforward to compute the absolute entropy by just choosing one of the state to have tractable thermodynamic properties.

The computational framework of Eqs. (2) and (3) is usually known as targeted free energy perturbation (TFEP) [28, 29]. Thanks to the rapid development of deep generative models in recent years, the desired invertible map f can now be efficiently represented by a class of generative models called normalizing flow [30], making TFEP emerge as a promising tool for free energy calculation [31–34]. In contrast to the “variational” approach, which has previously been applied to a broad range of many-body problems [32, 33, 35–39], the flow matching method we employ in this work represents a different training scheme of the flow model [23–25], which offers a variety of advantages in both accuracy and efficiency; see Supplemental Material [27] for details.

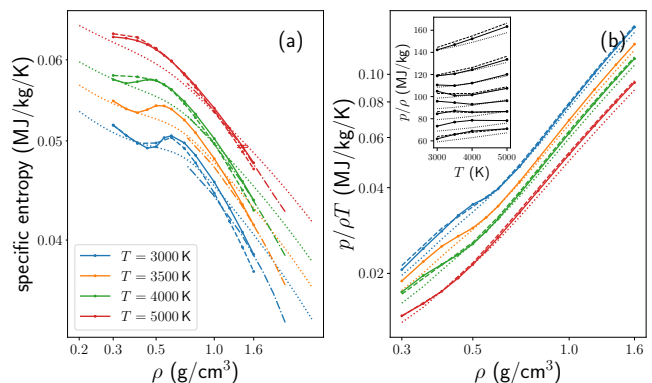


FIG. 1. (a) Specific entropy s and (b) pressure p (scaled by ρT) as a function of density ρ for several isotherms. Solid line: the present work using flow matching method; dotted line: CMS19 [11]; dashed line: REOS3 [14]; dash-dotted line: the entropy reported by Morales *et al.* [19] based on CEIMC simulations. Note the REOS3 entropy has been globally *shifted* to align with our results; see text for details. The inset of (b) presents the same pressure data by selected isochores, with density ranging from 0.3 (bottom) to 0.7 g/cm³ (up).

Entropy from ab initio data. We employ the flow matching method to study the *ab initio* portion of the phase diagram, with $3000 \leq T \leq 8000$ K and $0.3 \leq \rho \leq 1.6$ g/cm³. Specifically, we repeatedly train a transformation f and use Eq. (2) to compute the entropy difference for each neighboring pair of states on a (T, ρ) grid; see Supplemental Material [27] for an example. We also calculate the *absolute* entropy of a reference state within the same framework and then shift the entropy of other states rigidly. In practice, we choose the reference point at $T = 5000$ K and $\rho = 1.4$ g/cm³ [27], where the computed value 0.0494(1) MJ/kg/K of the absolute entropy is in excellent agreement with those reported by Morales *et al.* [19] based on coupled electron-ion Monte Carlo (CEIMC) simulations.

Figure 1 shows our results (solid line) for several isotherms of the specific entropy s and pressure p , together with two widely used hydrogen EOSs in past literature: CMS19 [11] (dotted line) and REOS3 [14] (dashed line). For convenience, we also include an error bar of absolute entropy at the reference point, and the CEIMC entropy of Morales *et al.* [19] (dash-dotted line) at relatively high densities. Note the REOS3 entropy is calculated by us using TI (see Eq. (1)), and, for sake of visualization, we have introduced a global entropy offset to make it match our data at the bottom-left phase point, i.e., $T = 3000$ K and $\rho = 0.3$ g/cm³. We do not compare with the MH13 EOS [12] since it is derived directly for hydrogen-helium mixtures.

One striking feature of Fig. 1(a) is the non-monotonic behavior of entropy at low temperatures in both our results and REOS3, which is qualitatively different from CMS19. Moreover, CMS19 does not feature the typical slope change of the $p - \rho$ relation, as shown in Fig. 1(b), which is emanating from the critical point of the liquid-liquid phase transition between molecular and atomic phase [40, 41]. This indicates

that although derived from DFT-PBE data in the phase region considered here [11, 19, 42, 43], the CMS19 EOS does not closely capture the pressure-induced molecular dissociation, which could have a notable impact on Jupiter models [27].

The observed behavior of entropy and pressure in our results, as described above, can be understood by virtue of the thermodynamic relation [21]: $(\partial s/\partial \rho)_T = -\rho^{-2}(\partial p/\partial T)_\rho$. In fact, by examining the pressure *isochores* as illustrated in the inset of Fig. 1(b), the region where the pressure *decreases* with temperature corresponds precisely to the region of *increasing* entropy in Fig. 1(a). Physically, they are just different manifestations of the molecular dissociation effects: the attractive force from broken molecular bonds can dominate the repulsion from kinetic motion, while the larger number of configurations involving only individual H atoms (compared to those with bound H₂-like pairs) can compensate for the smaller occupied volume caused by increasing density.

Benchmarking thermodynamic integration. We can use the flow matching entropy to benchmark the TI approach, which simply amounts to integrating Eq. (1) using our pressure and energy data. We find that the TI entropies are virtually indistinguishable from the solid lines in Fig. 1(a). Besides, they do not depend on the choice of integration path and hence show very good thermodynamic consistency. Contrary to the previous belief [12], our observations indicate that TI performs quite well for a discrete grid with spacings in the order of 1000 K and 0.1g/cm³. When combined with the absolute entropy calculation on only a *single* referent point, as done above, we can then achieve the same level of accuracy as the “full” CCI approach in Ref. [12], but with far less computational costs.

Note that compared to REOS3, we have added some additional simulation points at relatively low densities to improve the characterization of molecular dissociation. Nevertheless, TI is not fundamentally flawed even with the relatively sparse grid of REOS3 in the *ab initio* region, and the resulting entropy remains generally consistent with our data, as shown by the dashed lines in Fig. 1(a). However, TI becomes truly problematic when we further extend the integration path to touch other regions based on inconsistent theories. We can quantitatively illustrate such inconsistency by performing the line integral $\oint d(F/T)$ along each closed local square loop of the tabular data, which should in principle vanish everywhere. However, for REOS3 we found large deviation from this ideal behavior between the *ab initio* region and the chemical model at lower densities [44, 45], as shown in Figure 2. This implies that the resulting entropy will be *ambiguously* defined and strongly depend on the choice of integration path and initial reference point; see Supplemental Material [27] for more details. One can then identify an entropy error of approximately 10% [27], which yields qualitatively large differences on planetary models derived in the past using this method [4, 13].

A thermodynamically consistent construction. We have shown that performing a single TI over an EOS containing various inconsistent theories can lead to significant and uncontrolled errors of the entropy. A better approach is to perform TI on each component (i.e., region where the same the-

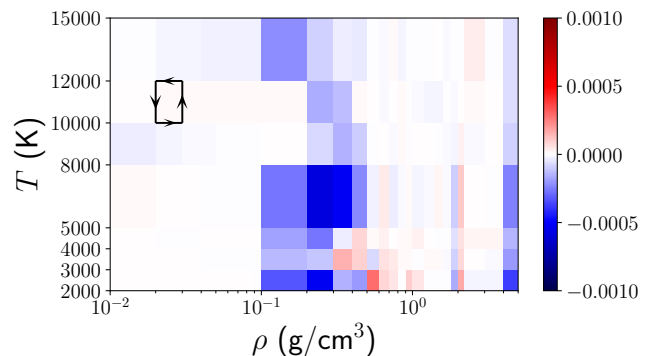


FIG. 2. The line integral $\oint d(F/T)$ (in unit of MJ/kg/K) computed along each closed local square loop of the REOS3 data. A schematic example of the loop is shown on the top-left corner.

ory applies) of the EOS *separately*, and then interpolate the resulting *free energy* function [27]. In this way, one can derive the pressure and energy near the interpolation boundaries by taking partial derivatives, which are naturally consistent by construction. Another advantage is that one can easily incorporate accurate values of the *absolute* entropy into each separate region. This ensures that any residual interpolation errors that one can make at the boundaries remain localized and do not propagate elsewhere.

Figure 3(a-d) show our final EOS (solid lines), which consist of the *ab initio* DFT-MD part at $\rho \geq 0.3\text{g/cm}^3$, the SCvH EOS at $\rho \leq 0.1\text{g/cm}^3$, and an interpolation region between them. For comparison, we also include the entropy and pressure isotherms of Miguel *et al.* [4] (dashed lines), which are obtained by a single TI over the entire phase region of REOS3. Note the new interpolation procedure depends very sensitively on the entropy difference between SCvH and the *ab initio* data [27]. In doing this, we then surprisingly found the reported (absolute) entropies of SCvH at room conditions (e.g., at standard pressure 1 bar and temperature 298.15K) are about 0.0057 MJ/kg/K (or $\sim 10\%$) higher than both the experimental data [46, 47] and theoretical calculations [48]. Only after such errors are fixed (by applying a global entropy shift on the SCvH side) can we achieve a high-quality interpolation that respects fundamental thermodynamic constraints; see Supplemental Material [27] for details. This observation, which results from totally independent experimental or numerical benchmarks at both low (~ 1 bar) and high ($\sim 700\text{GPa}$) pressures, is a very strong evidence on the accuracy of our construction. Fig. 3(e) also shows the local loop integral values $\oint d(F/T)$ of our final EOS; compared to Fig. 2, one clearly sees the new interpolation approach can indeed yield much better thermodynamic consistency over the entire phase diagram, as discussed above.

Jupiter’s adiabat. We demonstrate the utility of the newly constructed hydrogen EOS by performing a preliminary calculation of Jupiter’s adiabat. We assume a homogeneous model with no compact core, and set a helium mass frac-

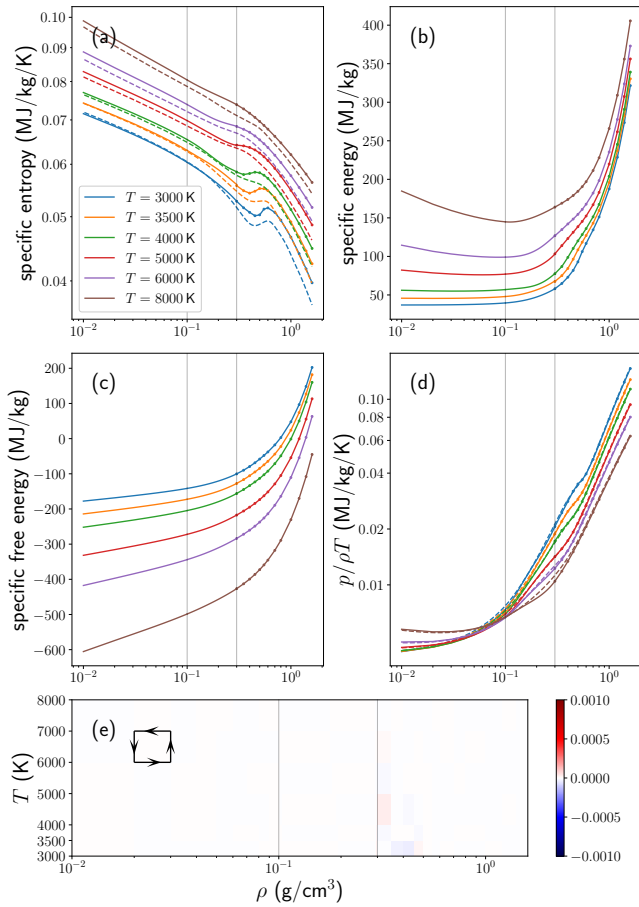


FIG. 3. Several (a) specific entropy, (b) specific energy, (c) specific free energy, and (d) pressure (scaled by ρT) isotherms of our final EOS (solid lines), which consist of the *ab initio* data at high densities, the SCvH EOS at low densities, and an interpolation region between them, as indicated by the vertical lines. The dashed lines are the entropy and pressure isotherms of Miguel *et al.* [4], obtained by performing a single TI over the entire phase region of REOS3. Note we have added an extra entropy shift of -0.0057 MJ/kg/K to both the dashed lines and SCvH part of the solid lines in panel (a) to align with the experimental data at low pressures; see text for details. Panel (e) shows the local loop integral values $\oint d(F/T)$ of our EOS, similar to Fig. 2 for the case of REOS3.

tion of $Y = 0.245$ to ensure a fair comparison with previous works [4, 12, 22]. We adopt a simple linear mixing approximation for the entropy of mixtures, using the REOS3 EOS of helium derived by Miguel *et al.* in Ref. [22]. The starting point is $p = 1$ bar and $T = 166.1$ K [1], which corresponds to an entropy (for hydrogen) of 0.043 MJ/kg/K.

Figure 4 shows our result for the adiabat (red dashed line), together with those derived from the REOS3 (black line) [22] and MH13 EOS (blue line) [12], respectively. For a comparison also with CMS19, see the Supplemental Material [27]. Note the hydrogen EOS used in the REOS3 adiabat was produced by Miguel *et al.* [4, 22] using a single TI over the entire phase region, as already shown by the dashed lines in Fig. 3. Our result clearly agrees well with the REOS3

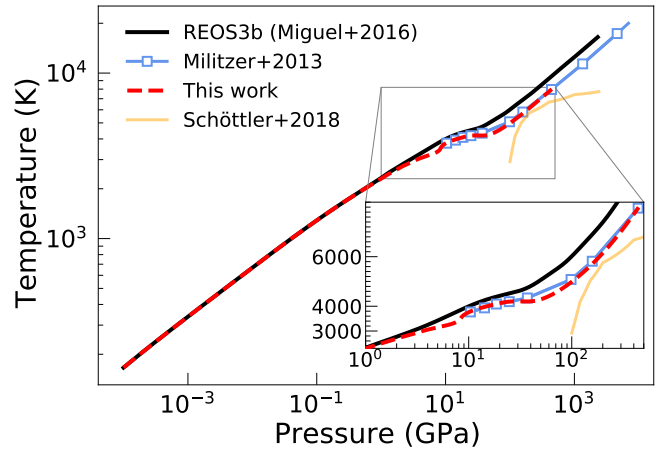


FIG. 4. Jupiter adiabat obtained from different EOSs. See text for a detailed comparison between our result (red dashed line) and those derived from the REOS3 (black line) [22] and MH13 EOS (blue line) [12]. The yellow line shows the hydrogen-helium demixing curve for a protosolar mixture from Ref. [49].

adiabat up to about 1 GPa, which is as expected since both the underlying hydrogen EOSs are derived at low pressures from the same SCvH model. However, at higher pressures, our adiabat begins to diverge from the REOS3 line and becomes cooler. This is a direct consequence of the systematically lower REOS3 entropy in the *ab initio* region in Fig. 3(a), which is in turn caused by the thermodynamic inconsistency shown in Fig. 2 [27]. Notice such a cooler adiabat passes very close to the miscibility boundary for hydrogen-helium mixtures, shown as the yellow line in Fig. 4, albeit derived from DFT-MD simulations using an exchange-correlation functional different from PBE [49]. This suggests an increased likelihood of phase separation between hydrogen and helium in Jupiter’s deep interior, causing the formation of so-called helium rain [1, 50, 51].

On the other hand, our adiabat at high pressures is apparently closer to the MH13 prediction, as shown by the blue line in Fig. 4. Note that the MH13 EOS is derived directly from *ab initio* MD simulations of a hydrogen-helium mixture and does not rely on the linear mixing approximation. Overall, we show that, at the DFT-PBE level of theory, the long-standing discrepancy between the Jupiter models of REOS3 and MH13 primarily stems from a problematic TI calculation of the REOS3 entropy that is not everywhere thermodynamically consistent. However, according to our earlier benchmark using flow matching, this definitely does *not* imply that TI is inherently inferior to the CCI approach for a finite number of simulation points, as speculated in Ref. [12]. Another observation from Fig. 4 is that the MH13 adiabat [12] was derived only for the *ab initio* region at high pressures. In fact, Ref. [12] did not really attempt a thermodynamically consistent interpolation with other regions to construct a complete EOS, which, however, is definitely needed for a thorough study of planetary models.

Summary and outlook. In this Letter, we closely examine the entropy calculation of dense hydrogen by benchmarking TI with an independent flow matching method. Based on this, we then construct a new hydrogen EOS that is both accurate and thermodynamically consistent over several orders of magnitude of pressure, which is crucial for reliable and conclusive planetary model predictions. Notably, the interpolation quality at the boundaries serves as a highly sensitive and stringent test for the accuracy of the theories on both sides [27]. Indeed, the new approach has allowed us to identify and correct a significant discrepancy in SCvH relative to experimental data at low pressures, which is fairly surprising and remarkable given the chemical model’s long history of nearly 30 years.

We conclusively address the long-standing issue of entropy disagreements among various popular EOSs used in planetary modeling [11, 12, 14], all of which are derived from the same DFT-PBE level of electronic structure theory. To further improve the hydrogen EOS and potentially reconcile models with observational data [5], one can upgrade the description of electronic correlation from DFT-PBE to a higher-level theory [39, 52–54]. We also note that as a generic tool, flow matching can also be used to study other rich phases of hydrogen [55, 56] or other interesting condensed matter systems [51, 57], where accurate calculation of free energy plays a significant role.

We acknowledge useful discussions with Lei Wang, Ravit Helled, Gilles Chabrier, and Armin Bergermann. We also acknowledge Cesare Cozza for providing initial data and support with the DFT calculations. H.X. and G.M. acknowledge financial support from the Swiss National Science Foundation (grant PCEFP2.203455). S.H. acknowledges financial support from the Swiss National Science Foundation (grant 200020.215634).

-
- [1] R. Helled, G. Mazzola, and R. Redmer, Understanding dense hydrogen at planetary conditions, *Nature Reviews Physics* **2**, 562 (2020).
- [2] T. V. Johnson, C. M. Yeates, and R. Young, Space science reviews volume on Galileo Mission overview, *Space Science Reviews* **60**, 3 (1992).
- [3] S. J. Bolton, J. Lunine, D. Stevenson, J. E. P. Connerney, S. Levin, T. C. Owen, F. Bagenal, D. Gautier, A. P. Ingersoll, G. S. Orton, T. Guillot, W. Hubbard, J. Bloxham, A. Coradini, S. K. Stephens, P. Mokashi, R. Thorne, and R. Thorpe, The Juno Mission, *Space Science Reviews* **213**, 5 (2017).
- [4] Miguel, Y., Guillot, T., and Fayon, L., Jupiter internal structure: the effect of different equations of state, *A&A* **596**, A114 (2016).
- [5] F. Debras and G. Chabrier, New Models of Jupiter in the Context of Juno and Galileo, *The Astrophysical Journal* **872**, 100 (2019).
- [6] Mazevet, S., Licari, A., and Soubiran, F., Benchmarking the ab initio hydrogen equation of state for the interior structure of jupiter, *A&A* **664**, A112 (2022).
- [7] Howard, S., Guillot, T., Bazot, M., Miguel, Y., Stevenson, D. J., Galanti, E., Kaspi, Y., Hubbard, W. B., Militzer, B., Helled, R., Nettelmann, N., Idini, B., and Bolton, S., Jupiter’s interior from Juno: Equation-of-state uncertainties and dilute core extent, *A&A* **672**, A33 (2023).
- [8] N. Nettelmann, N. Movshovitz, D. Ni, J. J. Fortney, E. Galanti, Y. Kaspi, R. Helled, C. R. Mankovich, and S. Bolton, Theory of Figures to the Seventh Order and the Interiors of Jupiter and Saturn, *The Planetary Science Journal* **2**, 241 (2021).
- [9] Miguel, Y., Bazot, M., Guillot, T., Howard, S., Galanti, E., Kaspi, Y., Hubbard, W. B., Militzer, B., Helled, R., Atreya, S. K., Connerney, J. E. P., Durante, D., Kulowski, L., Lunine, J. I., Stevenson, D., and Bolton, S., Jupiter’s inhomogeneous envelope, *A&A* **662**, A18 (2022).
- [10] B. Militzer, W. B. Hubbard, S. Wahl, J. I. Lunine, E. Galanti, Y. Kaspi, Y. Miguel, T. Guillot, K. M. Moore, M. Parisi, J. E. P. Connerney, R. Helled, H. Cao, C. Mankovich, D. J. Stevenson, R. S. Park, M. Wong, S. K. Atreya, J. Anderson, and S. J. Bolton, Juno Spacecraft Measurements of Jupiter’s Gravity Imply a Dilute Core, *The Planetary Science Journal* **3**, 185 (2022).
- [11] G. Chabrier, S. Mazevet, and F. Soubiran, A new equation of state for dense hydrogen–helium mixtures, *The Astrophysical Journal* **872**, 51 (2019).
- [12] B. Militzer and W. B. Hubbard, Ab initio equation of state for hydrogen–helium mixtures with recalibration of the giant-planet mass–radius relation, *The Astrophysical Journal* **774**, 148 (2013).
- [13] N. Nettelmann, A. Becker, B. Holst, and R. Redmer, Jupiter models with improved ab initio hydrogen equation of state (h-reos.2), *The Astrophysical Journal* **750**, 52 (2012).
- [14] A. Becker, W. Lorenzen, J. J. Fortney, N. Nettelmann, M. Schöttler, and R. Redmer, Ab initio equations of state for hydrogen (h-reos.3) and helium (he-reos.3) and their implications for the interior of brown dwarfs, *The Astrophysical Journal Supplement Series* **215**, 21 (2014).
- [15] J. P. Perdew, K. Burke, and M. Ernzerhof, Generalized gradient approximation made simple, *Phys. Rev. Lett.* **77**, 3865 (1996).
- [16] J. G. Kirkwood, Statistical Mechanics of Fluid Mixtures, *The Journal of Chemical Physics* **3**, 300 (1935).
- [17] G. A. de Wijs, G. Kresse, and M. J. Gillan, First-order phase transitions by first-principles free-energy calculations: The melting of al, *Phys. Rev. B* **57**, 8223 (1998).
- [18] D. Frenkel and B. Smit, *Understanding Molecular Simulation: From Algorithms to Applications*, 3rd ed. (Academic Press, 2023).
- [19] M. A. Morales, C. Pierleoni, and D. M. Ceperley, Equation of state of metallic hydrogen from coupled electron-ion monte carlo simulations, *Phys. Rev. E* **81**, 021202 (2010).
- [20] A. Bergermann, M. French, and R. Redmer, Ab initio calculation of the miscibility diagram for mixtures of hydrogen and water, *Phys. Rev. B* **109**, 174107 (2024).
- [21] D. Saumon, G. Chabrier, and H. M. van Horn, An Equation of State for Low-Mass Stars and Giant Planets, *Astrophysical Journal Supplement* **99**, 713 (1995).
- [22] Miguel, Y., Guillot, T., and Fayon, L., Jupiter internal structure: the effect of different equations of state (corrigendum), *A&A* **618**, C2 (2018).
- [23] M. S. Albergio and E. Vanden-Eijnden, Building normalizing flows with stochastic interpolants, in *The Eleventh International Conference on Learning Representations* (2023).
- [24] Y. Lipman, R. T. Q. Chen, H. Ben-Hamu, M. Nickel, and M. Le, Flow matching for generative modeling, in *The Eleventh International Conference on Learning Representations* (2023).
- [25] X. Liu, C. Gong, and qiang liu, Flow straight and fast: Learning to generate and transfer data with rectified flow, in *The Eleventh International Conference on Learning Representations* (2023).

- [26] L. Zhao and L. Wang, Bounding free energy difference with flow matching, *Chinese Physics Letters* **40**, 120201 (2023).
- [27] See Supplemental Material for more details on the theoretical formulations of targeted free energy perturbation and flow matching, as well as their implementation and some illustrative examples in practice. There are also further discussions about the effects of thermodynamic inconsistency on entropy calculation, our new EOS construction approach, and the comparison between Jupiter’s adiabats derived from various hydrogen EOSs.
- [28] C. Jarzynski, Targeted free energy perturbation, *Phys. Rev. E* **65**, 046122 (2002).
- [29] A. M. Hahn and H. Then, Using bijective maps to improve free-energy estimates, *Phys. Rev. E* **79**, 011113 (2009).
- [30] G. Papamakarios, E. Nalisnick, D. J. Rezende, S. Mohamed, and B. Lakshminarayanan, Normalizing flows for probabilistic modeling and inference, *Journal of Machine Learning Research* **22**, 1 (2021).
- [31] P. Wirnsberger, A. J. Ballard, G. Papamakarios, S. Abercrombie, S. Racanière, A. Pritzel, D. Jimenez Rezende, and C. Blundell, Targeted free energy estimation via learned mappings, *The Journal of Chemical Physics* **153**, 144112 (2020).
- [32] P. Wirnsberger, G. Papamakarios, B. Ibarz, S. Racanière, A. J. Ballard, A. Pritzel, and C. Blundell, Normalizing flows for atomic solids, *Machine Learning: Science and Technology* **3**, 025009 (2022).
- [33] R. Ahmad and W. Cai, Free energy calculation of crystalline solids using normalizing flows, *Modelling and Simulation in Materials Science and Engineering* **30**, 065007 (2022).
- [34] A. Molina-Taborda, P. Cossio, O. Lopez-Acevedo, and M. Gabrié, Active Learning of Boltzmann Samplers and Potential Energies with Quantum Mechanical Accuracy, *Journal of Chemical Theory and Computation* **20**, 8833 (2024).
- [35] S.-H. Li and L. Wang, Neural network renormalization group, *Phys. Rev. Lett.* **121**, 260601 (2018).
- [36] D. Wu, L. Wang, and P. Zhang, Solving statistical mechanics using variational autoregressive networks, *Phys. Rev. Lett.* **122**, 080602 (2019).
- [37] H. Xie, L. Zhang, and L. Wang, Ab-initio study of interacting fermions at finite temperature with neural canonical transformation, *Journal of Machine Learning* **1**, 38 (2022).
- [38] H. Xie, L. Zhang, and L. Wang, m^* of two-dimensional electron gas: A neural canonical transformation study, *SciPost Phys.* **14**, 154 (2023).
- [39] H. Xie, Z.-H. Li, H. Wang, L. Zhang, and L. Wang, Deep variational free energy approach to dense hydrogen, *Phys. Rev. Lett.* **131**, 126501 (2023).
- [40] W. Lorenzen, B. Holst, and R. Redmer, First-order liquid-liquid phase transition in dense hydrogen, *Phys. Rev. B* **82**, 195107 (2010).
- [41] H. Y. Geng, Q. Wu, M. Marqués, and G. J. Ackland, Thermodynamic anomalies and three distinct liquid-liquid transitions in warm dense liquid hydrogen, *Phys. Rev. B* **100**, 134109 (2019).
- [42] L. Caillabet, S. Mazevet, and P. Loubeyre, Multiphase equation of state of hydrogen from ab initio calculations in the range 0.2 to 5 g/cc up to 10 ev, *Phys. Rev. B* **83**, 094101 (2011).
- [43] B. Holst, R. Redmer, and M. P. Desjarlais, Thermophysical properties of warm dense hydrogen using quantum molecular dynamics simulations, *Phys. Rev. B* **77**, 184201 (2008).
- [44] H. Juranek, R. Redmer, and Y. Rosenfeld, Fluid variational theory for pressure dissociation in dense hydrogen: Multicomponent reference system and nonadditivity effects, *The Journal of Chemical Physics* **117**, 1768 (2002).
- [45] B. Holst, N. Nettelmann, and R. Redmer, Equation of state for dense hydrogen and plasma phase transition, *Contributions to Plasma Physics* **47**, 368 (2007).
- [46] J. D. Cox, D. D. Wagman, and V. A. Medvedev, Codata key values for thermodynamics, in *Series on Thermodynamic Properties* (1989).
- [47] E. W. Lemmon, I. H. Bell, M. L. Huber, and M. O. McLinden, Thermophysical properties of fluid systems, in *NIST Chemistry WebBook, NIST Standard Reference Database Number 69*, edited by P. Linstrom and W. Mallard (National Institute of Standards and Technology, Gaithersburg MD, 20899, 2023).
- [48] NIST Computational Chemistry Comparison and Benchmark Database, NIST Standard Reference Database Number 101 (2022).
- [49] M. Schöttler and R. Redmer, Ab initio calculation of the miscibility diagram for hydrogen-helium mixtures, *Phys. Rev. Lett.* **120**, 115703 (2018).
- [50] J. Vorberger, I. Tamblyn, B. Militzer, and S. A. Bonev, Hydrogen-helium mixtures in the interiors of giant planets, *Phys. Rev. B* **75**, 024206 (2007).
- [51] X. Chang, B. Chen, Q. Zeng, H. Wang, K. Chen, Q. Tong, X. Yu, D. Kang, S. Zhang, F. Guo, Y. Hou, Z. Zhao, Y. Yao, Y. Ma, and J. Dai, Theoretical evidence of h-he demixing under jupiter and saturn conditions, *Nature Communications* **15**, 8543 (2024).
- [52] C. Pierleoni, M. A. Morales, G. Rillo, M. Holzmann, and D. M. Ceperley, Liquid-liquid phase transition in hydrogen by coupled electron-ion monte carlo simulations, *Proceedings of the National Academy of Sciences* **113**, 4953 (2016).
- [53] G. Mazzola, R. Helled, and S. Sorella, Phase diagram of hydrogen and a hydrogen-helium mixture at planetary conditions by quantum monte carlo simulations, *Phys. Rev. Lett.* **120**, 025701 (2018).
- [54] K. Nakano, C. Attaccalite, M. Barborini, L. Capriotti, M. Casula, E. Coccia, M. Dagrada, C. Genovese, Y. Luo, G. Mazzola, A. Zen, and S. Sorella, TurboRVB: A many-body toolkit for ab initio electronic simulations by quantum Monte Carlo, *The Journal of Chemical Physics* **152**, 204121 (2020).
- [55] M. A. Morales, C. Pierleoni, E. Schwegler, and D. M. Ceperley, Evidence for a first-order liquid-liquid transition in high-pressure hydrogen from ab initio simulations, *Proceedings of the National Academy of Sciences* **107**, 12799 (2010).
- [56] H. Niu, Y. Yang, S. Jensen, M. Holzmann, C. Pierleoni, and D. M. Ceperley, Stable solid molecular hydrogen above 900 k from a machine-learned potential trained with diffusion quantum monte carlo, *Phys. Rev. Lett.* **130**, 076102 (2023).
- [57] X. Wang, Z. Wang, P. Gao, C. Zhang, J. Lv, H. Wang, H. Liu, Y. Wang, and Y. Ma, Data-driven prediction of complex crystal structures of dense lithium, *Nature Communications* **14**, 2924 (2023).
- [58] R. W. Zwanzig, High-Temperature Equation of State by a Perturbation Method. I. Nonpolar Gases, *The Journal of Chemical Physics* **22**, 1420 (1954).
- [59] C. H. Bennett, Efficient estimation of free energy differences from monte carlo data, *Journal of Computational Physics* **22**, 245 (1976).
- [60] R. T. Q. Chen, Y. Rubanova, J. Bettencourt, and D. Duvenaud, Neural ordinary differential equations, in *Proceedings of the 32nd International Conference on Neural Information Processing Systems, NIPS’18* (Curran Associates Inc., Red Hook, NY, USA, 2018) p. 6572–6583.
- [61] L. Zhang, W. E, and L. Wang, Monge-ampère flow for generative modeling (2018), [arXiv:1809.10188 \[cs.LG\]](https://arxiv.org/abs/1809.10188).
- [62] A. Vaswani, N. Shazeer, N. Parmar, J. Uszkoreit, L. Jones, A. N. Gomez, L. u. Kaiser, and I. Polosukhin, Attention is all you

- need, in *Advances in Neural Information Processing Systems*, Vol. 30, edited by I. Guyon, U. V. Luxburg, S. Bengio, H. Wallach, R. Fergus, S. Vishwanathan, and R. Garnett (Curran Associates, Inc., 2017).
- [63] J. Köhler, L. Klein, and F. Noé, Equivariant flows: sampling configurations for multi-body systems with symmetric energies (2019), [arXiv:1910.00753 \[stat.ML\]](https://arxiv.org/abs/1910.00753).
- [64] V. G. Satorras, E. Hoogeboom, and M. Welling, E(n) equivariant graph neural networks, in *Proceedings of the 38th International Conference on Machine Learning*, Proceedings of Machine Learning Research, Vol. 139, edited by M. Meila and T. Zhang (PMLR, 2021) pp. 9323–9332.
- [65] M. Taddei, M. Ruggieri, S. Moroni, and M. Holzmann, Iterative backflow renormalization procedure for many-body ground-state wave functions of strongly interacting normal fermi liquids, *Phys. Rev. B* **91**, 115106 (2015).
- [66] D. Pfau, J. S. Spencer, A. G. D. G. Matthews, and W. M. C. Foulkes, Ab initio solution of the many-electron schrödinger equation with deep neural networks, *Phys. Rev. Res.* **2**, 033429 (2020).
- [67] G. Pescia, J. Han, A. Lovato, J. Lu, and G. Carleo, Neural-network quantum states for periodic systems in continuous space, *Phys. Rev. Res.* **4**, 023138 (2022).
- [68] M. Wilson, S. Moroni, M. Holzmann, N. Gao, F. Wudarski, T. Vegge, and A. Bhowmik, Neural network ansatz for periodic wave functions and the homogeneous electron gas, *Phys. Rev. B* **107**, 235139 (2023).
- [69] G. Cassella, H. Sutterud, S. Azadi, N. D. Drummond, D. Pfau, J. S. Spencer, and W. M. C. Foulkes, Discovering quantum phase transitions with fermionic neural networks, *Phys. Rev. Lett.* **130**, 036401 (2023).
- [70] G. Pescia, J. Nys, J. Kim, A. Lovato, and G. Carleo, Message-passing neural quantum states for the homogeneous electron gas, *Phys. Rev. B* **110**, 035108 (2024).
- [71] P. Giannozzi, S. Baroni, N. Bonini, M. Calandra, R. Car, C. Cavazzoni, D. Ceresoli, G. L. Chiarotti, M. Cococcioni, I. Dabo, A. Dal Corso, S. de Gironcoli, S. Fabris, G. Fratesi, R. Gebauer, U. Gerstmann, C. Gougoussis, A. Kokalj, M. Lazzeri, L. Martin-Samos, N. Marzari, F. Mauri, R. Mazzarello, S. Paolini, A. Pasquarello, L. Paulatto, C. Sbraccia, S. Scandolo, G. Sclauzero, A. P. Seitsonen, A. Smogunov, P. Umari, and R. M. Wentzcovitch, Quantum espresso: a modular and open-source software project for quantum simulations of materials, *Journal of Physics: Condensed Matter* **21**, 395502 (19pp) (2009).
- [72] P. E. Blöchl, Projector augmented-wave method, *Phys. Rev. B* **50**, 17953 (1994).
- [73] H. J. Monkhorst and J. D. Pack, Special points for brillouin-zone integrations, *Phys. Rev. B* **13**, 5188 (1976).
- [74] G. Bussi, D. Donadio, and M. Parrinello, Canonical sampling through velocity rescaling, *The Journal of Chemical Physics* **126**, 014101 (2007).
- [75] R. T. Q. Chen and Y. Lipman, Flow matching on general geometries, in *The Twelfth International Conference on Learning Representations* (2024).
- [76] L. Klein, A. Krämer, and F. Noe, Equivariant flow matching, in *Thirty-seventh Conference on Neural Information Processing Systems* (2023).
- [77] H. W. Kuhn, The hungarian method for the assignment problem, *Naval Research Logistics Quarterly* **2**, 83 (1955).
- [78] B. Militzer, Equation of state calculations of hydrogen-helium mixtures in solar and extrasolar giant planets, *Phys. Rev. B* **87**, 014202 (2013).
- [79] A. Becker, N. Nettelmann, B. Holst, and R. Redmer, Isentropic compression of hydrogen: Probing conditions deep in planetary interiors, *Phys. Rev. B* **88**, 045122 (2013).
- [80] M. A. Morales, J. M. McMahon, C. Pierleoni, and D. M. Ceperley, Nuclear quantum effects and nonlocal exchange-correlation functionals applied to liquid hydrogen at high pressure, *Phys. Rev. Lett.* **110**, 065702 (2013).
- [81] G. Chabrier and A. Y. Potekhin, Equation of state of fully ionized electron-ion plasmas, *Phys. Rev. E* **58**, 4941 (1998).
- [82] B. Militzer and D. M. Ceperley, Path integral monte carlo calculation of the deuterium hugoniot, *Phys. Rev. Lett.* **85**, 1890 (2000).
- [83] B. Militzer and D. M. Ceperley, Path integral monte carlo simulation of the low-density hydrogen plasma, *Phys. Rev. E* **63**, 066404 (2001).

SUPPLEMENTAL MATERIAL

Consider a hydrogen system composed of N protons and N electrons in a periodic box of volume L^3 . By introducing the dimensionless Wigner-Seitz parameter $r_s = (3/4\pi N)^{1/3}L/a_0$, where a_0 is the Bohr radius, one can then write the mass density (in unit of g/cm^3) of the system as $\rho = 2.69467/r_s^3$. Let $(T_0, \rho_0), (T_1, \rho_1)$ be two state points on the temperature-density phase diagram, the corresponding Boltzmann distributions then read $p_i(\mathbf{x}) = e^{-\beta_i E_i(\mathbf{x})}/Z_i$ ($i = 0, 1$), respectively. $\mathbf{x} \equiv (\mathbf{r}_1, \dots, \mathbf{r}_N)$ denotes the proton coordinates, $\beta_i = 1/k_B T_i$, and k_B is the Boltzmann constant. $Z_i = \int d\mathbf{x} e^{-\beta_i E_i(\mathbf{x})}$ is known as the partition function and directly related to the Helmholtz free energy $F_i = -\frac{1}{\beta_i} \ln Z_i$.

In this work, we use the flow matching method to benchmark the calculation of free energy difference (scaled by temperature) between the two states, $\beta_1 F_1 - \beta_0 F_0 = -\ln Z_1/Z_0$, against the conventional thermodynamic integration (TI) approach. Below we will discuss various aspect of the new method, including the underlying theoretical framework, training objectives, implementation details, and some illustrative examples of the results.

Targeted free energy perturbation

In contrast to TI, flow matching is built on the framework of targeted free energy perturbation (TFEP) [28, 29], as already mentioned in the main text. Compared to the original free energy perturbation based on importance sampling [58], TFEP further leverages an invertible map in the configuration space to significantly increase state overlap and thereby reduces the variance of relevant estimators.

More specifically, consider a map f that transforms coordinate samples $\mathbf{x} \sim p_0(\mathbf{x})$ of the state 0 into a new state $0'$, whose probability density function is given by the change-of-variables formula:

$$\begin{aligned} p'_{0'}(\mathbf{x}) &= p_0(f^{-1}(\mathbf{x})) \left| \det \left(\frac{\partial f^{-1}(\mathbf{x})}{\partial \mathbf{x}} \right) \right| \\ &= \frac{1}{Z_0} e^{-\beta_0 E_0(f^{-1}(\mathbf{x}))} \left| \det \left(\frac{\partial f^{-1}(\mathbf{x})}{\partial \mathbf{x}} \right) \right| \\ &= \frac{1}{Z_0} e^{-\beta_0 E'_0(\mathbf{x})}, \end{aligned} \quad (\text{S1})$$

where the transformed ‘‘energy function’’ is defined as

$$E'_0(\mathbf{x}) = E_0(f^{-1}(\mathbf{x})) - \frac{1}{\beta_0} \ln \left| \det \left(\frac{\partial f^{-1}(\mathbf{x})}{\partial \mathbf{x}} \right) \right|. \quad (\text{S2})$$

Similarly, the inverse of f would transform the state 1 to a new state $1'$ with energy function

$$E'_1(\mathbf{x}) = E_1(f(\mathbf{x})) - \frac{1}{\beta_1} \ln \left| \det \left(\frac{\partial f(\mathbf{x})}{\partial \mathbf{x}} \right) \right|. \quad (\text{S3})$$

In practice, one would like to find an appropriate f such that the transformed state $0'(1')$ has significant overlap with the

target state $1(0)$. Based on the idea of importance sampling, the free energy difference can then be efficiently estimated as follows:

$$\begin{aligned} \beta_1 F_1 - \beta_0 F_0 &= -\ln \frac{Z_1}{Z_0} \\ &= -\ln \mathbb{E}_{\mathbf{x} \sim p_0(\mathbf{x})} \left[e^{-\Phi_{\rightarrow}(\mathbf{x})} \right] = \ln \mathbb{E}_{\mathbf{x} \sim p_1(\mathbf{x})} \left[e^{\Phi_{\leftarrow}(\mathbf{x})} \right], \end{aligned} \quad (\text{S4})$$

where

$$\begin{aligned} \Phi_{\rightarrow}(\mathbf{x}) &= \beta_1 E'_1(\mathbf{x}) - \beta_0 E_0(\mathbf{x}) \\ &= \beta_1 E_1(f(\mathbf{x})) - \beta_0 E_0(\mathbf{x}) - \ln \left| \det \left(\frac{\partial f(\mathbf{x})}{\partial \mathbf{x}} \right) \right|, \end{aligned} \quad (\text{S5a})$$

$$\begin{aligned} \Phi_{\leftarrow}(\mathbf{x}) &= \beta_1 E_1(\mathbf{x}) - \beta_0 E'_0(\mathbf{x}) \\ &= \beta_1 E_1(\mathbf{x}) - \beta_0 E_0(f^{-1}(\mathbf{x})) + \ln \left| \det \left(\frac{\partial f^{-1}(\mathbf{x})}{\partial \mathbf{x}} \right) \right| \end{aligned} \quad (\text{S5b})$$

are known as the *forward* and *reverse* work, respectively. These results are precisely the Eqs. (2) and (3) in the main text.

Note that due to limited number of samples in practice, the two estimators in Eq. (S4) are actually biased, which can be readily demonstrated using Jensen’s inequality [29]. Specifically, the estimator involving the forward (reverse) work turns out to be an upper (lower) bound of the true free energy difference value. The extent of bias will, of course, depend on the quality of the map f . In this work, we found these two bounds are generally quite tight; see the sections below for some illustrative examples. As a result, we choose to simply perform an arithmetic mean of the two bounds to generate the final data, although some more sophisticated and potentially superior approaches may also be considered [59]. Another observation is that the estimation of *absolute* entropy appears to be more straightforward within the TFEP framework compared to TI: once one of the two states is chosen to have tractable entropy, the practical implementation remains almost unchanged.

Flow matching

As mentioned in the main text, one appealing feature of the TFEP estimators in Eq. (S4) is that they depend solely on samples from the two end states, as opposed to TI which requires information along an entire path. The price one pays, however, is the design of a suitable map f , which is often challenging and lack of generic physical guidelines. This is arguably the main reason why the TFEP framework has not been widely used in realistic problems since its introduction.

The recent progress in the field of deep generative modeling has largely changed the situation. Specifically, the desired invertible map can be efficiently represented by a class of generative models called normalizing flow [30], making TFEP reemerge as a promising tool for free energy calculation. In previous attempts [31–34], the training objectives

have been exclusively based on variants of the Kullback-Leibler (KL) divergence, which provide direct access to the free energy difference as a variational upper or lower bound. This *variational* training scheme has been successfully applied to a broad range of physical problems, including lattice models [35, 36], atomic solids [32, 33], quantum dots [37], uniform electron gases [38], and also dense hydrogen [39]. However, it still has some drawbacks for the present purpose. First, the training process typically requires a large number of energy calculations of the underlying system, which would be time-consuming for *ab initio* methods like DFT. As a result, many works have used empirical [31–33] or machine-learned potentials [34], which would inevitably introduce new source of errors. Second, symmetry constraints often play an essential role in the efficient training of flow model, especially for systems like pure hydrogen. Although several neural network designs have been proposed to meet various symmetry requirements [31, 32], they are still not satisfactory enough regarding a proper balance between the expressive power and computational cost. The continuous normalizing flow (CNF) [60, 61] is arguably the most convenient and flexible candidate now to incorporate symmetries, but its variational training requires expensive numerical integrations of ordinary differential equation (ODE) and scales unfavorably for large system sizes.

The recently developed flow matching method [23–25] has largely overcome these difficulties. More specifically, one can smoothly connect the two end probability distributions $p_0(\mathbf{x})$, $p_1(\mathbf{x})$ by introducing an interpolant $I_t(\mathbf{x}_0, \mathbf{x}_1)$, where $t \in [0, 1]$ is a continuous “time” parameter, such as

$$I_{t=0}(\mathbf{x}_0, \mathbf{x}_1) = \mathbf{x}_0, \quad I_{t=1}(\mathbf{x}_0, \mathbf{x}_1) = \mathbf{x}_1. \quad (\text{S6})$$

The essence is that the velocity field $\mathbf{v}_t(\mathbf{x})$ underlying such an interpolated “probability path” can then be obtained by minimization of the following objective:

$$\mathcal{L} = \mathbb{E}_{t \sim [0,1]} \mathbb{E}_{\mathbf{x}_0 \sim p_0(\mathbf{x}_0)} \mathbb{E}_{\mathbf{x}_1 \sim p_1(\mathbf{x}_1)} |\mathbf{v}_t(I_t(\mathbf{x}_0, \mathbf{x}_1)) - \partial_t I_t(\mathbf{x}_0, \mathbf{x}_1)|^2. \quad (\text{S7})$$

Notice this expression requires only samples from the two end distributions; there are not any on-the-fly evaluation of configurational energy or ODE integration during the training stage. On the other hand, these types of costly computations are indeed present when estimating the free energy difference after the training is finished, as shown in Eqs. (S4) and (S5). In particular, the transformed coordinates $f(\mathbf{x})$ and corresponding log-Jacobian determinant $\ln |\det(\partial f / \partial \mathbf{x})| \equiv \ln J_f(\mathbf{x})$ should be evaluated by jointly integrating the following set of ODEs [60, 61]:

$$\frac{d\mathbf{x}}{dt} = \mathbf{v}_t(\mathbf{x}), \quad \frac{d \ln J_f}{dt} = \nabla \cdot \mathbf{v}_t(\mathbf{x}). \quad (\text{S8})$$

However, it should be noted that such computations are performed only once and thus still practically affordable.

As mentioned above, compared to previous network designs for discrete flow model [31, 32], the incorporation of

various symmetries can also be more convenient for continuous normalizing flow. Specifically, the invariance of probability distribution can simply be achieved by requiring the underlying velocity field to be *equivariant* under the desired symmetry operation \mathcal{P} :

$$\mathbf{v}_t(\mathcal{P}\mathbf{x}) = \mathcal{P}\mathbf{v}_t(\mathbf{x}). \quad (\text{S9})$$

To do this in practice, we can leverage many recent advances in various areas, such as natural language processing [62], molecular simulation [31, 63], graph neural networks [64], and quantum many body computations [38, 39, 65–70].

Implementation details

The MD generation of coordinate samples used for training Eq. (S7) and the energy computation appearing in the free energy estimators Eq. (S4) are both performed in the DFT level using the QUANTUM ESPRESSO code [71]. We use the exchange-correlation functional of Perdew, Burke and Ernzerhof (PBE) [15] and the pseudopotential of projector-augmented wave [72] type. We choose the system size $N = 128$, and the \mathbf{k} -space integration is performed on a $3 \times 3 \times 3$ Monkhorst-Pack grid [73]. The energy cutoff for the plane wave basis set and charge densities are 80 and 800 Ry, respectively. These parameters have been checked to yield well converged energetics. For MD simulations, the ion temperature is controlled using stochastic-velocity rescaling [74] and the time step is set to 12 a.u..

The network we use for the velocity field $\mathbf{v}_t(\mathbf{x})$ is adapted from FermiNet [66], which is permutation and translation equivariant by construction. We also modify the pair distance features to comply with the periodic nature of the simulation box [38, 67–69]. We choose a simple linear interpolating function

$$I_t(\mathbf{x}_0, \mathbf{x}_1) = (1 - t)\mathbf{x}_0 + t\mathbf{x}_1, \quad (\text{S10})$$

with the caveat in mind that we are working on a periodic box. This setting turns out to be equivalent to the Riemannian flow matching on a torus as proposed in Ref. [75]. To allow for more efficient use of the training data, we choose to further incorporate permutation symmetry explicitly into the flow matching objective Eq. (S7) itself [76]. In practice, this can be achieved by finding the permutation with minimal distance for each pair $\mathbf{x}_0, \mathbf{x}_1$ of samples using the Hungarian algorithm [77].

Illustrative examples of the results

To showcase the utility of TFEP and flow matching in practice, we consider as a typical example the two end states with $T_0 = 3000\text{K}$, $\rho_0 = 0.5\text{g/cm}^3$ and $T_1 = 3000\text{K}$, $\rho_1 = 0.55\text{g/cm}^3$, respectively. These states are near the molecular dissociation where the radial distribution function changes

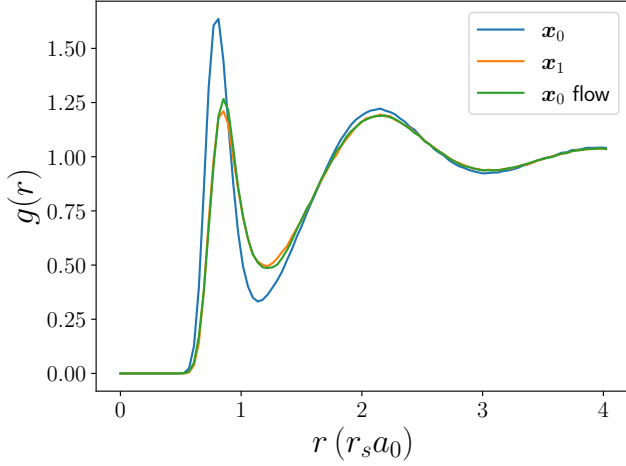


FIG. S1. Radial distribution functions of the two states at $T_0 = 3000\text{K}$, $\rho_0 = 0.5\text{g/cm}^3$ and $T_1 = 3000\text{K}$, $\rho_1 = 0.55\text{g/cm}^3$, respectively. The line labeled with “ x_0 flow” represents the new state obtained by transforming samples of state 0 using the velocity field trained with flow matching.

dramatically, as shown in Figure S1. Note we have measured the distance in terms of $r_s a_0$; under such a scale, the simulation box size is $(4\pi N/3)^{1/3}$ and does not depend on the density of the system. This would facilitate the interpolation between the two Boltzmann distributions as done in the flow matching method. Fig. S1 also shows the radial distribution function of the new state transformed from state 0, obtained by integrating the first ODE in Eq. (S8) using the trained velocity field. The result is clearly very close to the target state 1, indicating a significant state overlap.

After the training is complete, one can further use Eq. (S4) to estimate the upper and lower bound of free energy difference between the two states, as shown by the red and black vertical line in Fig. S2, respectively. The distance between these two bounds is roughly within their own error bars, which implies our estimation have been tight enough. Figure S2 also shows histograms for the distribution of forward and reverse work Φ_{\rightarrow} , Φ_{\leftarrow} as defined in Eq. (S5). The significant overlap between these two work distributions indicates the high quality of the trained velocity field in effectively connecting the two end states being considered. Furthermore, one can clearly see the estimated free energy difference values coincide well with the intersection point of the two work distributions, where the probability densities are equal. This is a direct consequence of the fluctuation theorem as derived in Ref. [29].

We also use the same workflow outlined above to calculate the *absolute* free energy and entropy of the reference state at $T = 5000\text{K}$ and $\rho = 1.4\text{g/cm}^3$, as mentioned in the main text. In practice, we choose the “tractable state” to correspond to a simple uniform distribution. The resulting radial distribution functions and free energy bounds are shown in Figures S3 and S4, respectively. Notice that in the present case, the two end

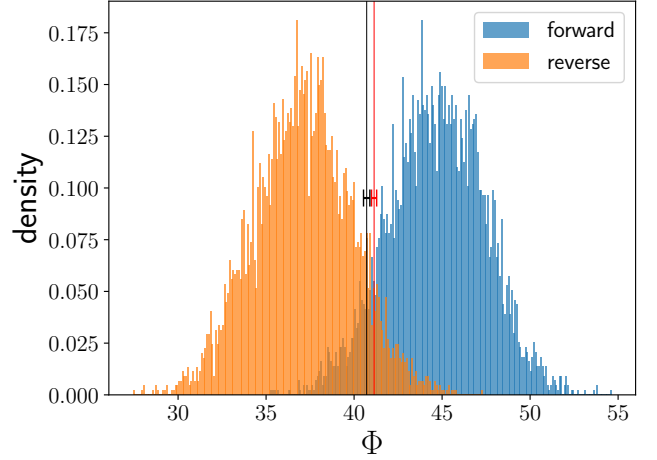


FIG. S2. Histograms for the distribution of forward and reverse work, defined in Eq. (S5), between the two states at $T_0 = 3000\text{K}$, $\rho_0 = 0.5\text{g/cm}^3$ and $T_1 = 3000\text{K}$, $\rho_1 = 0.55\text{g/cm}^3$. The vertical red (black) line is the estimated upper (lower) bound for free energy difference; see Eq. (S4) and the discussions therein.

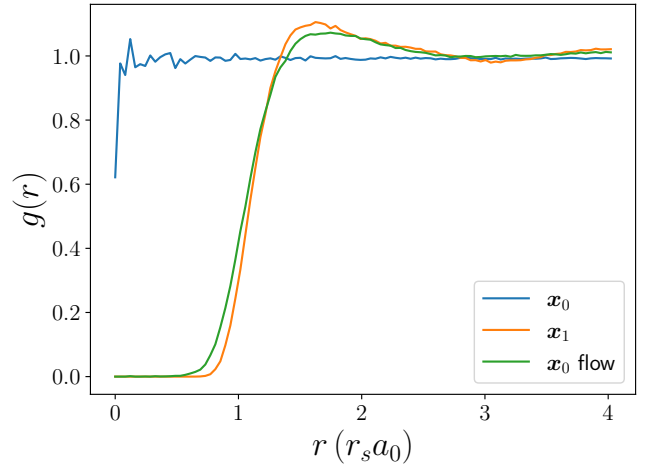


FIG. S3. Same as Fig. S1, except the states 0 and 1 correspond to the uniform distribution and the reference state at $T = 5000\text{K}$, $\rho = 1.4\text{g/cm}^3$, respectively.

states differ more substantially than those in Fig. S1, making the flow matching training of the velocity field more challenging. As a result, the forward and reverse work distributions also have less overlap, and the upper and lower bounds for the free energy difference are less tight compared to Fig. S2. Nonetheless, the absolute entropy of the reference state can still be estimated with a relative error of 0.2%, which is comparable to the results reported by Morales *et al.* [19] using Hamiltonian thermodynamic integration and already satisfactory for the present purpose (see Fig. 1(a) in the main text).

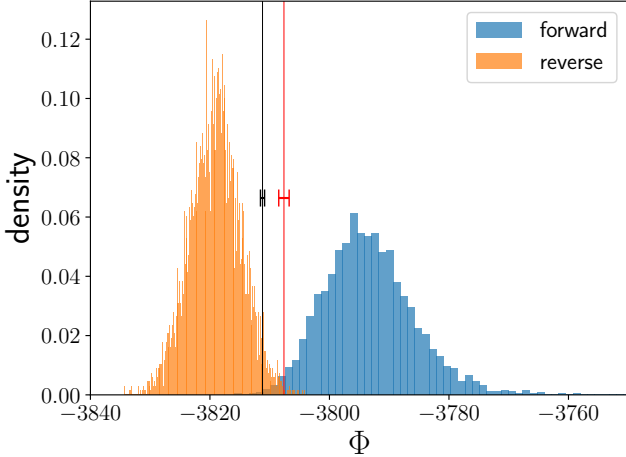


FIG. S4. Same as Fig. S2, except the states 0 and 1 correspond to the uniform distribution and the reference state at $T = 5000\text{K}$, $\rho = 1.4\text{g/cm}^3$, respectively.

Effect of thermodynamic inconsistency on entropy calculation

In Fig. 2 of the main text, we have shown the entropy calculated by a single TI over the entire phase region of REOS3 can be thermodynamically inconsistent in the intermediate region between different theories. By comparing the maximum value 10^{-3}MJ/kg/K of the color bar in Fig. 2 to the scale of Fig. 1(a) in the main text, one can conclude that a local inconsistency of such a magnitude will likely lead to significant discrepancy of the entropy. To illustrate this, we compute the REOS entropy by integrating either along the isotherm or isochore first, as shown by the red and blue solid lines in Figure S5, respectively. Note for a given grid of points, we have selected the one with lowest temperature and density as the reference point for integration. One can see for a large phase region (the main panel of Fig. S5) that covers both the chemical model and *ab initio* data, the results from the two integration paths begin to diverge significantly at intermediate densities, which is a direct consequence of the inconsistency observed in Fig. 2 of the main text. On the other hand, such a divergence becomes nearly negligible when the integration is performed exclusively over the *ab initio* region, as shown in the inset of Fig. S5.

The subtleties involved in the implementation of TI arise not only from different choices of integration path, but also the reference point. In fact, the latter can be seen as an alternative manifestation of the former, which can be understood by noting that an integration path can belong to different types (i.e., isotherm or isochore first) when viewed by different reference points. As an illustration, Fig. S5 also shows the entropy reported by Miguel *et al.* [4] (dashed lines). According to the authors, they processed the original REOS3 data by integrating along isotherm first, hence in accordance with the red solid lines of our result. However, these two sets of entropies clearly differ by an offset in the *ab initio* region of the

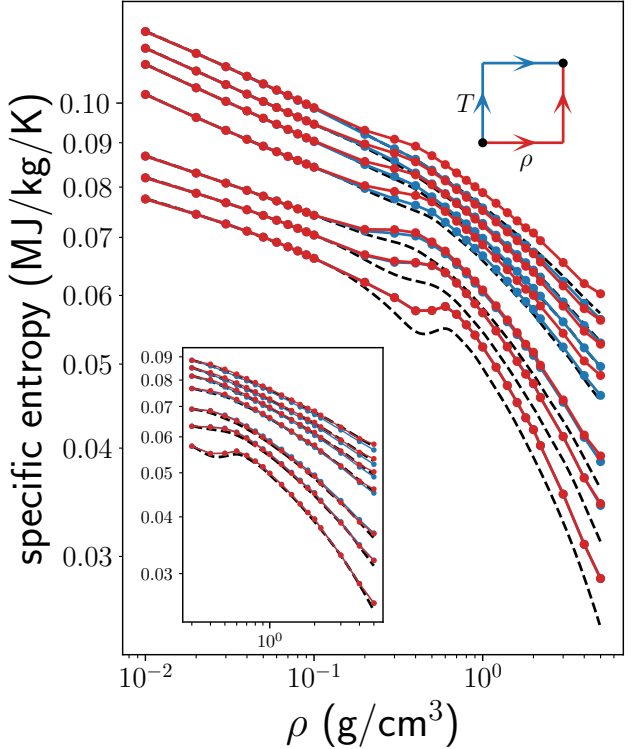


FIG. S5. Several specific entropy isotherms of REOS3 computed by TI over a wide density range ($0.01 \leq \rho \leq 5\text{g/cm}^3$, main panel) and only the *ab initio* region at high densities ($\rho \geq 0.3\text{g/cm}^3$, inset). The corresponding temperatures for the isotherms are (from bottom to top) 3000, 4000, 5000, 8000, 10000, 12000, and 15000K. The red (blue) solid lines correspond to the results of integrating along isochore (isotherm) first, as schematically illustrated on the top-right corner. For both regions, the reference point is set to the one with lowest temperature and density. The dashed lines are the entropy data produced by Miguel *et al.* [4].

main panel. The remedy of such an apparent disagreement turns out to be surprisingly easy: notice all the entropy isochores already align well, we just need to locate the reference point on another “correct” isotherm, say, 15000K. After doing this, the red solid lines then coincide perfectly with the dashed lines from Ref. [4], as shown in Figure S6.

Our reproduction of the entropy results by Miguel *et al.* [4] based on a specific integration path and reference point, as done above, demonstrates how fragile the “global” TI approach can be for an EOS with significant thermodynamic inconsistencies. Notice the solid and dashed lines in Fig. S5 differ by roughly 10%, which can make a big difference on planetary model predictions as shown in the main text.

More details on the thermodynamically consistent construction of our EOS

To construct an EOS that is thermodynamically consistent across several distinct theories, such as *ab initio* DFT and

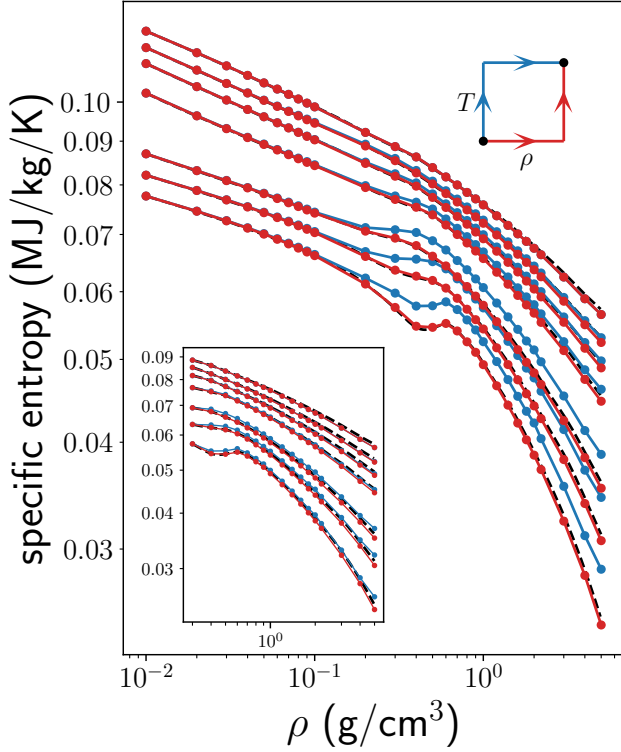


FIG. S6. Same as Fig. S5, except the reference point (for TI calculation of the solid lines) is set to be at $T = 15000\text{K}$ and the lowest density.

SCvH, one needs to first calculate the free energy and entropy of each region *separately* using the standard TI approach. We then perform a two-dimensional spline interpolation over each set of free energy data, following a similar approach to Militzer and Hubbard [12]. This in principle allows us to reproduce the original pressure and energy data by performing partial derivatives. The quality of such reproduction is, of course, closely related to the original level of thermodynamic consistency in each region. Once the free energy interpolation for each separate region is ready, we can then glue them together by performing another spline interpolation along their boundaries. Note one can utilize relevant partial derivative values derived from the free energy interpolations on both sides to ensure a smoother connection.

In this work, we attempted an interpolation between the *ab initio* DFT-PBE data at $\rho \geq 0.3\text{g/cm}^3$ and the SCvH EOS at $\rho \leq 0.1\text{g/cm}^3$. Note we have chosen the locations of the density boundaries based on reasonable assumptions about the range of validity of both theories. Intuitively speaking, the size of the intermediate density gap reflects a trade-off between our confidence in available (but potentially conflicting) data and the flexibility to perform interpolations between them.

In principle, the free energy interpolation would be perfectly smooth if the absolute entropy and energy (measured relative to the same baseline) were exact on both sides. How-

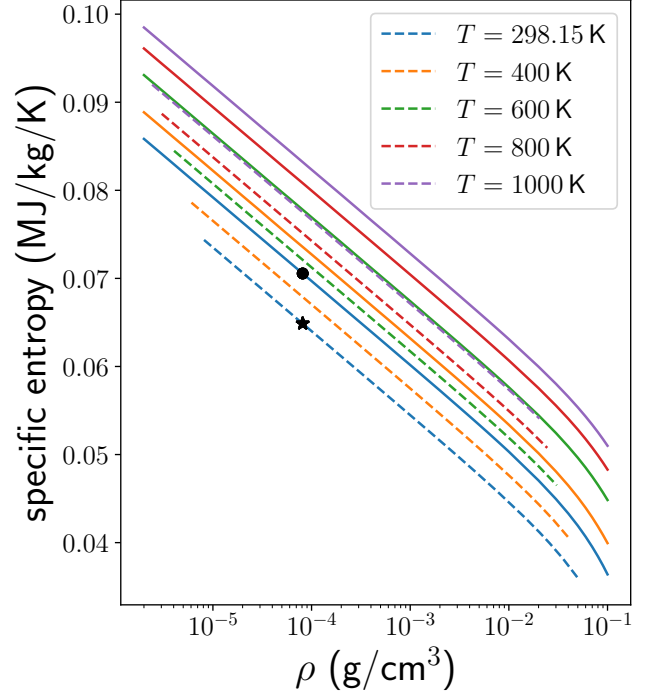


FIG. S7. Several specific entropy isotherms of hydrogen at room conditions from the SCvH EOS [21] (solid lines) and experimental data [46, 47] (dashed lines). The black markers correspond to the standard condition (1 bar, 298.15K).

ever, this is not the case in practice. First, it is generally believed that only the *relative energies* produced by DFT (using any given exchange-correlation functional) are reliable, rather than the absolute ones. This indicates that we are allowed to globally shift the DFT energies as we want, which, of course, leaves the entropy (and any other thermodynamic properties) unchanged. Second, we have surprisingly found the SCvH entropies are about 0.0057 MJ/kg/K (or $\sim 10\%$) higher than well-established experimental data at room conditions [46, 47], as mentioned in the main text. As shown in Figure S7, this discrepancy between the two sets of data is fairly uniform across a broad region of (low) temperatures and densities, including the standard condition (1 bar, 298.15K) that has been marked explicitly.

To get a feeling of the impact such an entropy error can have on the interpolation, Figure S8 shows the resulting EOS using the *original* (but incorrect) SCvH entropy data. Note that although we have selected an DFT energy offset to connect the free energy isotherms on both sides as smoothly as possible (see panel (c)), there still remains a noticeable mismatch. On the other hand, Fig. S8(d) shows the interpolated pressure is also apparently problematic. In particular, the wild wiggle behavior at the intermediate densities can even cause violation of the basic mechanical stability constraint $(\partial p/\partial \rho)_T > 0$ [21] and hence definitely *unphysical*.

Notice that in Fig. S8(c), the free energy isotherms of SCvH appear to be *wider* than the *ab initio* region. Recalling the ba-

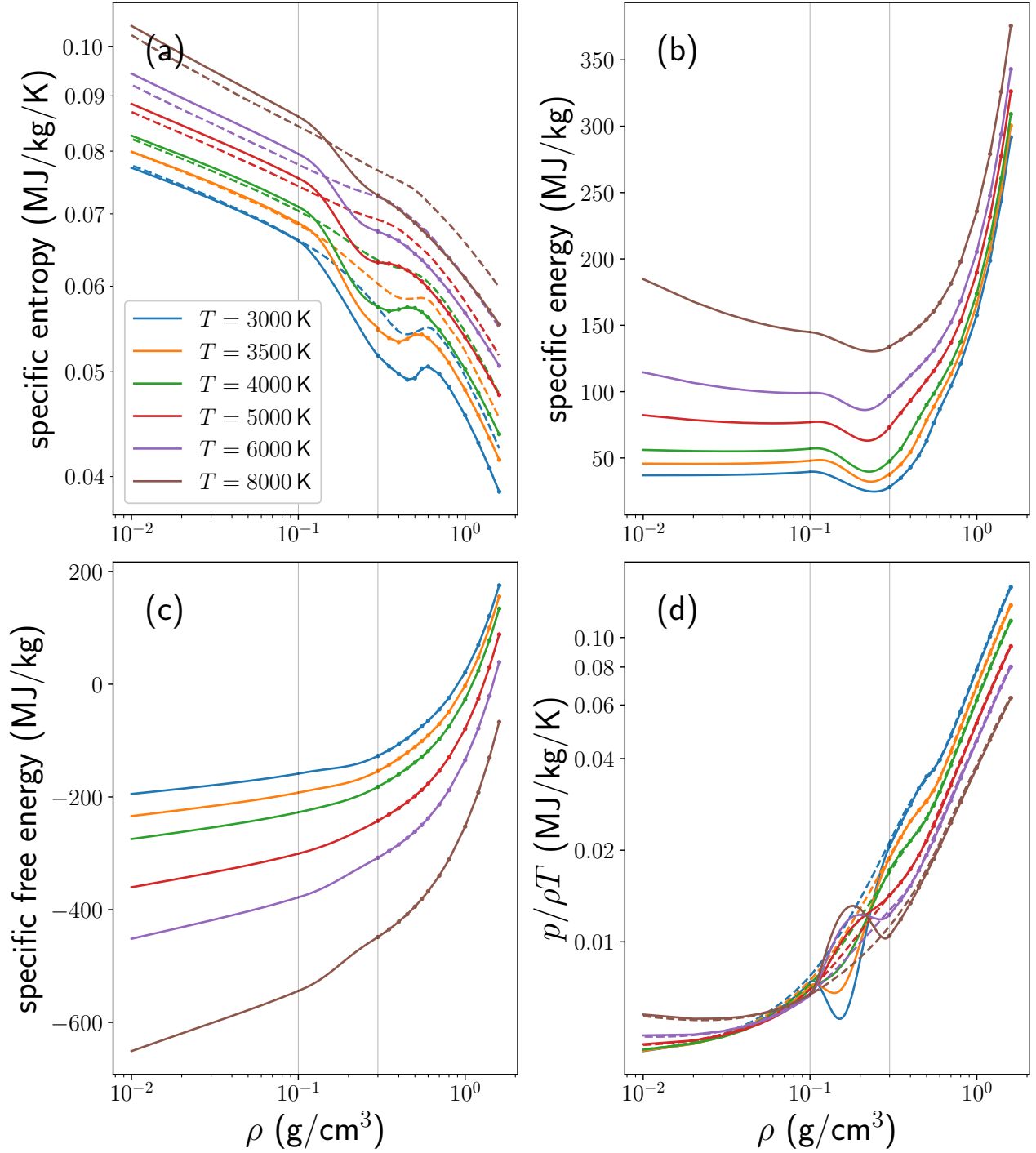


FIG. S8. The hydrogen EOS (solid lines) constructed in the same way as Fig. 3 in the main text, except that the *original* (but incorrect) absolute entropy of the SCvH EOS is used. The dashed lines are the original entropy and pressure isotherms of Miguel *et al.* [4], obtained by performing a single TI over the entire phase region of REOS3.

sic relation $F = E - TS$, the problematic interpolation can then be remedied by globally *reducing* the SCvH entropy to match the correct experimental value. This leads to the final EOS shown in Fig. 3 of the main text. Note we have also added an extra entropy offset of 0.001 MJ/kg/K on the DFT side to

make the interpolation look slightly better. Nevertheless, this residual error is much smaller than the SCvH entropy error discussed above and does not affect our essential arguments on the accuracy and reliability of the new EOS construction approach.

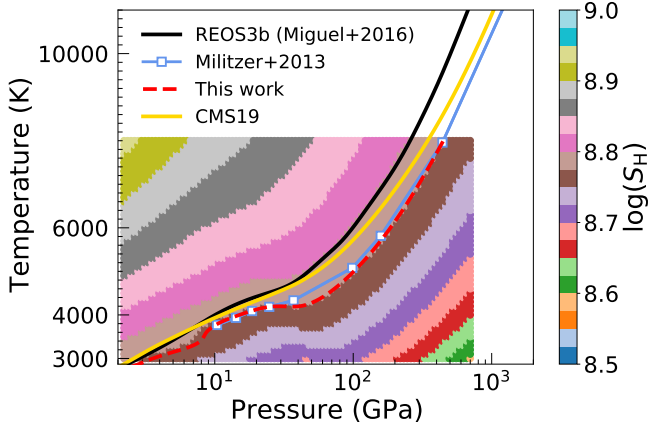


FIG. S9. Jupiter adiabats obtained from different EOSs. Compared to Fig. 4 of the main text, we also additionally show the adiabat derived from the CMS19 EOS [11], as well as the entropy of our EOS by colored regions.

In principle, the remaining small error near the interpolation boundaries can be eliminated by using more accurate chemical models at low densities or electron structure methods (such as QMC) at high densities. Besides, the nuclear quantum effect may also have a slight impact on the *ab initio* entropy at low temperatures, which has been ignored in this work. This can be remedied either by adding some semi-empirical corrections [78, 79] or resorting to more accurate (and also more costly) path integral MD simulations [80].

More details of comparison between different Jupiter’s adiabats

Figure S9 shows some more details of Jupiter’s adiabats calculated using various hydrogen EOSs. Compared to Fig. 4 of the main text, there is additionally the adiabat derived from the CMS19 EOS [11] (yellow line), which is clearly *smoother* in the *ab initio* region than both our result (red dashed line) and MH13 (blue line). This difference originates from the significant, non-monotonic slope change of our entropy isotherms, as shown in Fig. 1(a) of the main text. In Fig. S9, we also directly illustrate the entropy of our EOS by colored regions. The change of slope is again clearly evident, indicating that our EOS better captures the pressure-induced molecular dissociation than CMS19.

By definition, our calculated adiabat (red dashed line) follows the shape of a certain “stripe” of constant entropy, as clearly shown in Fig. S9. Note that the slightly imperfect behavior of our adiabat between 1 and 10GPa corresponds to the interpolation region of our EOS; see the previous section for more discussions. However, it is worth emphasizing that this remaining error will not affect the accuracy and reliability of our adiabat at higher pressures, where the disagreements between various adiabats make the biggest difference on resulting planetary model predictions [4, 7].

In Fig. S9, our adiabat is confined to the *ab initio* region explored in this work, specifically up to $T = 8000\text{K}$ and $\rho = 1.6\text{g/cm}^3$. It is in principle just a matter of additional DFT-MD simulations or interpolations with other theories [21, 81–83] to extend the hydrogen EOS to higher temperatures and densities. This will enable us to accurately study Jupiter’s deeper interior beyond the red dashed line in Fig. S9, or other astrophysical objects under even more extreme conditions, such as solar-type stars.